Speciation and chemical behavior of molybdenum in uranium dioxide samples prepared by hydroxide precipitation

Mohammad Husainy, Stéphanie Szenknect, Renaud Podor, Xavier Le Goff, Thibault Kaczmarek, Philippe Moisy, Nicolas Dacheux

Journal of Nuclear Materials 596 (2024) 155075

Contents lists available at ScienceDirect

Journal of Nuclear Materials

journal homepage: www.elsevier.com/locate/jnucmat

Speciation and chemical behavior of molybdenum in uranium dioxide samples prepared by hydroxide precipitation

Mohammad Husainy [a], Stéphanie Szenknect [a,*], Renaud Podor [a], Xavier Le Goff [a], Thibault Kaczmarek [a], Philippe Moisy [b], Nicolas Dacheux [a]

[a] ICSM, Univ Montpellier, CEA, CNRS, ENSCM, Site de Marcoule, Bagnols-sur-Cèze, France
[b] CEA, DES, ISEC, DMRC, Univ Montpellier, Site de Marcoule, Bagnols-sur-Cèze, France

ARTICLE INFO

Keywords:
Molybdenum
Uranium dioxide
Hydroxide precipitation, Sintering
Structure
Microstructure

ABSTRACT

This work aims to investigate the behavior of Mo in $UO_{2\pm x}$ for being an abundant fission product with a high fission yield and a complex speciation linked to its interaction with the fuel and other fission product elements. UO_2-based model compounds containing different Mo contents (between 0 and 15 mol%) were synthesized by a wet-chemistry route using hydroxide precipitation. The recovered powders were converted to oxides, pelletized, and sintered to obtain densified pellets of UO_2 incorporating Mo. PXRD analyses and Rietveld refinement calculations indicate that Mo has an almost negligible solubility in the fluorite structures of both UO_2 and UO_{2+x} samples. SEM, TEM, and EDX characterizations of the produced UO_2 + Mo pellets revealed the homogeneous distribution of nanosized metallic Mo particles of spherical geometry inside and outside the UO_2 grains and throughout the whole sample pellets, whatever the amount of Mo added, thus confirming that the solubility of Mo in the fluorite structure is way below 0.6 mol% Mo in accordance with the PXRD results. The microstructural properties of the UO_2 + Mo pellets, including density, porosity, Mo particle size distribution, and UO_2 grain size variation with Mo content, were also determined. The addition of Mo to UO_2 reduced the UO_2 grain size as compared to UO_2 grains in pure pellets, and Mo thus plays an inhibiting role in the UO_2 grain growth during sintering. The produced UO_2 + Mo pellets exhibit a microstructure similar to that of the real spent nuclear fuel, except that the UO_2 grains are smaller. The Mo metallic nanoparticles in these simplified UO_2-based model compounds of controlled microstructure could be harnessed as surrogates of the Mo-rich ε-phase metallic nanoparticles in the real spent nuclear fuel for future studies.

1. Introduction

Knowledge of the chemical state of fission products (FPs) and the phases formed in irradiated fuels is of prime importance for the waste management of spent nuclear fuels, whether dissolved in nitric acid for reprocessing of U and Pu or stored in deep geological repositories for final disposal. The irradiated UO_2 fuel forms a multicomponent system consisting of more than 40 FPs that can be distributed among several phases depending on irradiation temperature, pressure, and burnup [1]. On the basis of numerous post-irradiation analyses, FPs were classified into volatile elements, elements forming metallic or oxide precipitates, and elements dissolving in the UO_2 fuel matrix [1–3]. Of all the FPs, Mo has a unique place and plays a significant role in the chemistry of reactor fuel. Mo is one of the most abundant FPs with a high fission yield equivalent to that of Xe [1–5], and its abundance alone would justify a detailed study of its behavior. In light water reactor conditions, the atomic fraction of Mo calculated by the ORIGEN-2 or CESAR code in a stoichiometric UO_2 fuel at burnups between 55 and 100 GWd.t^{-1} ranges approximately between 1 and 2 mol%, respectively [6]. Moreover, Mo is considered to have a large influence on the fuel dioxygen potential, for the dioxygen potential of the couple Mo/MoO_2 is very close to that expected in a stoichiometric UO_2 fuel [1,7]. Mo therefore provides an important buffering capacity on UO_2 dioxygen potential, or equivalently, a sensitive indicator of fuel oxidation state [1,5–8].

It is well-known that Mo is a FP that can form both metallic and oxide precipitates within the UO_2 matrix. To elucidate, Mo associates with Tc, Rh, Ru, and Pd to form a noble metal phase, known as the ε-phase, with Mo and Ru being the major constituents of the alloy phase in most cases

* Corresponding author.
E-mail address: stephanie.szenknect@cea.fr (S. Szenknect).

https://doi.org/10.1016/j.jnucmat.2024.155075
Received 16 January 2024; Received in revised form 19 March 2024; Accepted 5 April 2024
Available online 15 April 2024

[1–9]. The five-metal particles mostly exhibit a hexagonal close packed structure and were identified by electron microscopy as white inclusions inside the UO_2 grains and within the grain boundaries but also within fission gas bubbles [1,9–12]. These metallic particles vary in diameter from a few micrometers to 5–20 nanometers, depending on their location in the fuel [9,11]. In addition, Mo is also identified in the oxidized state in Cs_2MoO_4 and in the so-called gray oxide phases, which are dominant perovskite precipitates within the fuel containing primarily oxides of Ba, U, Pu, Zr and Mo [1,5].

The solubility of Mo in UO_2 was investigated in several studies, and the reported results are hitherto contradictory. In 1985, H. Kleykamp [1] studied the solubility of several FPs in the fluorite structure, including Mo. UO_2 pellets containing 2 wt% Mo were annealed at 2173 K for 15 h under Ar high pressures in sealed capsules, and the solubility of Mo was measured by X-ray microanalysis. A maximum solubility of 0.006 mol% Mo in UO_2 was proposed at 2173 K, which was at the detection limit for Mo by the used analytical technique [1,13]. This negligible solubility is in accordance with an earlier study conducted by C. Giacchetti and C. Sari [14], who suggested a maximum solubility of about 0.06 mol% Mo at temperatures between 1773 and 2873 K in a mixed-oxide fuel $(U_{0.85}Pu_{0.15})O_{2\pm x}$ by electron probe microanalysis (EPMA), independent of fuel stoichiometry. In 2004, P. Martin et al. [8] carried out X-ray absorption near-edge structure (XANES) measurements on fresh UO_2 pellets implanted with Mo ions and annealed at 1273 K under a reducing atmosphere of Ar + 5 % H_2. The experimental observations indicated that Mo would be present in a metallic form or in a standard Schottky defect in the case of stoichiometric $UO_{2.00}$ fuel. However, in the case of hyper-stoichiometric UO_{2+x} fuel, Mo would be oxidized, and a fraction of the Mo ions could be located in the cationic sites, in agreement with the computer simulations of S. Nicoll et al. [7]. This led the authors to conclude that the Mo solubility in UO_2 was likely higher than Kleykamp's value of 0.006 mol%, but the extent of the higher Mo solubility predicted was not quantified. In 2010, Y.K. Ha et al. [15] prepared UO_2 pellets containing different contents of Mo between 0 and 15 mol% by dry chemistry route from mixtures of U_3O_8 and MoO_2 powders, followed by sintering at 1973 K for 12 h and annealing at 1473 K for 12 h under H_2 reducing atmosphere. A maximum solubility of 4 mol% Mo in UO_2 was quoted by observing a homogeneous UO_2 phase at the macroscopic scale for compositions lower than 4 mol% Mo and a phase separation by Mo precipitates at higher contents. It was also suggested that Mo could be present in Schottky-type defects and that the fluorite structure of UO_2 would be preserved with possible variations in the lattice parameter depending on the Mo content. Nevertheless, the authors did not exclude the possibility of the formation of Mo nanometric precipitates for contents below 4 mol%, which were probably not detected during the electron probe microanalyses [15]. A recent study by L. Sarrasin et al. [16,17] about the mechanisms of incorporation and migration of Mo in UO_2 and UO_{2+x} matrices showed that Mo can fit in the uranium vacancies of both networks and that its position is stabilized by the surrounding oxygen atoms, based on density functional theory (DFT) calculations of the electronic structure. In 2018, a thermodynamic review by E.C. Corcoran et al. [18] of the U-Mo-O ternary system reassessed the solubility limit of Mo in UO_2 at the same temperatures as the previously cited works. The established thermochemical model (TCM) predicts a solubility of 0.12 mol% Mo at 2173 K higher than the limit measured by H. Kleykamp [1], 0.1 mol% Mo at 1973 K much lower than the threshold proposed by Y.K. Ha et al. [15], and 0.01 mol% Mo at 1273 K in line with the study of P. Martin et al. [8]. Furthermore, a more recent study by M. Khair et al. [19] of the Mo solubility in UO_2 as a function of dioxygen partial pressure at 1373 K proposes a threshold of about 0.03 mol% Mo, which lied at the detection limit of Mo by the secondary ion mass spectroscopy (SIMS) used for this measurement.

Accordingly, the Mo solubility in UO_2 is partial, ranging between 0,006 and 4 mol%, and the position(s) occupied by Mo within the fuel structure should be studied. The previously studied samples were either prepared by dry chemistry route from mixtures of U and Mo powder precursors or by direct ionic implementation of Mo in UO_2, followed by thermal treatments under different oxidizing or reducing atmospheres. The latter techniques have shown large discrepancies in terms of Mo distribution within the final fuel oxide as well as in the particle size distribution. In the framework of this study, we used the original wet-chemistry protocol described by J. Martinez et al. [20] to prepare a variety of UO_2 pellets with diverse Mo contents by hydroxide precipitation. Such a wet-chemistry route leads to better homogeneity of the elements in the starting mixture compared to that obtained by co-grinding of powders or by ionic implementation, which would improve the physicochemical properties of the material. The question regarding the solubility of Mo and its behavior within the UO_2 fuel matrix was re-evaluated in light of the obtained experimental results.

2. Experimental

2.1. Preparation of uranium dioxide pellets with different Mo contents

Uranium oxide compounds of desired Mo contents between 0 and 15 mol% were synthesized using the hydroxide precipitation route developed by J. Martinez et al. [20]. The preparation of the initial hydroxide precursors consisted in mixing solutions of concentrated uranium (IV) chloride (0.6 mol.L^{-1} in 4 mol.L^{-1} HCl) and molybdenum (III) chloride (0.05 mol.L^{-1} in 1 mol.L^{-1} HCl) at the desired stoichiometric ratio Mo/(U + Mo). Each mixture was then poured into a large excess of ammonia solution leading to the instantaneous precipitation of the elements at room temperature. The formed precipitate was further aged in solution for 30 min under magnetic stirring in air. Afterwards, the precipitated powder was separated from the supernatant by centrifugation at 4500 rpm and then washed twice with distilled water and once with ethanol in order to remove any remaining traces of ammonia. The recovered powders were introduced into an Ar glove box and left to dry for one week. The hydroxide powder precursors comprising U and Mo were converted into oxides in a single calcination step at 1073 K for 4 h under a reducing atmosphere of Ar + 4 % H_2 ($pO_2 \approx 10^{-29}$ atm measured on line with JOK'AIR oxygen analyzer, SETNAG). The latter step allowed the complete dehydration of the hydroxide samples and their full conversion into oxides, as described in the protocol [20].

The chemical composition of each sample was determined by inductively coupled plasma atomic emission spectroscopy (ICP-AES) after the complete dissolution of a weighed amount of the converted oxide powder in 5 mL of 4 mol.L^{-1} HNO_3 at 353 K and then analyzing the U and Mo elemental concentrations in the obtained solution that was further diluted in 0.2 mol.L^{-1} HNO_3. The supernatants collected during the synthesis washing steps were also analyzed by ICP-AES to determine the precipitation yield of both U and Mo cations. The intensity of the emitted spectral signal was recorded at three characteristic wavelengths for each element: $\lambda = 202.030$, 203.844 and 204,598 nm for Mo and $\lambda =$ 367.007, 385.958 and 409.014 nm for U to avoid interferences between the emission spectra of the elements. The measurements were calibrated by analyzing mixed U and Mo standard solutions prepared by diluting 1000 ppm reference certified solutions in 0.2 mol.L^{-1} HNO_3. The concentration of U and Mo elements in solution was calculated from the average concentration of at least three replicates.

The synthesized oxide samples of verified compositions used to prepare pellets in this study contained 0, 0.6, 2, 4, 6, 9, and 15 mol% Mo. The calcinated oxide powders were first ground in an agate mortar with a pestle then compacted using a 5 mm dry-pellet die set of tri-shells followed by uniaxial hydraulic pressing at 500 MPa. The cylindrical green pellets produced with a 50 % densification rate were all 1–2 mm in height and approximately 200 mg in mass. Several pellets of each composition were sintered separately at 1873 K for 6 h in an Ar + 4 % H_2 reducing atmosphere.

2.2. Characterization of samples

Structural characterization of the oxide powders obtained after calcination at 1073 K for 4 h and of crushed parts from the sintered pellets at 1873 K for 6 h under reducing atmosphere was carried out by powder X-ray diffraction (PXRD). Samples were ground in a mortar and then mounted on Si wafers of zero background effect in confined specimen holders with dome-like X-ray transparent caps having knife-edge beam stops. The PXRD patterns were recorded on a Bruker D8 Advance diffractometer equipped with a LYNXEYE detector in parallel beam geometry with Göbel Mirror configuration using Cu $K\alpha_{1,2}$ radiation of $\lambda_{average} = 1.5418$ Å. The data were collected at ambient conditions in an angular range 2θ between 5 and 100°, with a step size of 0.019°, and a total counting time of about 3 h. The produced PXRD patterns were refined by the Rietveld method using the GSAS-II software package [21] to identify the phases present in the prepared urania and the potential structural changes in the presence of different Mo contents.

The density of the sintered pellets was determined by coupled geometric and pycnometric measurements using a digital precision caliper and a He gas pycnometer (Micrometrics AccuPyc II 1345), respectively. From geometric measurements, the bulk density (d_{geo}) of each pellet was evaluated and compared to the calculated density (d_{calc}) accounting for Mo additives, thereby leading to the determination of densification rates. Furthermore, measurements by He pycnometry allowed the determination of the effective density (d_{pycno}) of the pellets and hence the closed porosity. The relative error on the density values reached 1–2 % and was propagated while determining the porosity values. The total porosity (P_{tot}), closed porosity (P_{closed}), and open porosity (P_{open}) were calculated according to the following equations:

$$P_{tot}(\%) = \left(1 - \frac{d_{geo}}{d_{calc}}\right) \times 100 \quad (1)$$

$$P_{closed}(\%) = \left(1 - \frac{d_{pycno}}{d_{calc}}\right) \times 100 \quad (2)$$

$$P_{open}(\%) = P_{tot} - P_{closed} \quad (3)$$

In addition, scanning electron microscope (SEM) characterization of the oxide powders and the sintered pellets was performed by an environmental scanning electron microscope (ESEM, FEI Quanta 200 ESEM FEG) using a backscattered electron detector (BSE) or a secondary electron detector (SE) in vacuum conditions at an optimal working distance of about 10 mm. The SEM micrographs of the oxide powders (deposition on carbon stickers) were recorded with a low accelerating voltage of 2 kV in order to create a beam deceleration effect leading to high-resolution images. The SEM micrographs for the inspection of Mo distribution in the pellets (surface and interior cut sections) were recorded directly without any additional sample preparation, such as metallization, with an accelerating voltage of about 10 kV. The chemical composition was further checked by energy dispersive X-ray spectroscopy (EDS) coupled with SEM using the same operating conditions.

The average grain size of UO_2 was calculated using the SEraMic method developed by R. Podor et al. [22], which was implemented in the SEraMic plugin for the Fiji software [23]. This method was performed by high-vacuum recording and processing of 5–10 BSE images of each selected zone at tilt angles varying between −5 and +5° to emphasize the crystallographic orientation contrast of the grains [22]. This required wet polishing of the sample to obtain a mirror-like surface using a series of SiC papers of different grades followed by a two-step final polishing with 1 μm diamond paste for 2 min and colloidal silica suspension for about 10 min. The samples were thereafter cleaned ultrasonically with ethanol for a few minutes. Each series of images was aligned and then binarized to extract an average segmented image representing the grain boundaries and pores. A set of typically 500–1000 grains was considered to statistically compute the grain size distribution in each sample with distinct Mo content.

SEM micrographs recorded at high magnification and low acceleration voltage of 3 kV under high vacuum were used to determine the size distribution of the Mo particles observed at the UO_2 pellet surface. These conditions allowed the creation of a beam deceleration effect, resulting in highly resolved images. The analyzed samples were polished to a mirror grade following the same polishing steps used for the SEraMic application. A collection of 3–5 BSE images from each sample were treated by the Trainable Weka Segmentation plugin [24] in Fiji, which combined machine learning algorithms with the selected images to produce pixel-based segmentations discriminating between Mo particles, UO_2 grains, and present pores. The pores identified as Mo particles were eliminated manually. The typical Mo particles considered for each sample from various selected zones ranged between 200 and 800 particles.

In order to verify the chemical nature of the observed Mo particles, electron-transparent ultra-fine cross sections of sintered pellets were cut using a FEI Helios 600 NanoLab Focused Ion Beam (FIB) available at CP2M (Aix-Marseille University, France). The FIB lamellae were then analyzed by transmission electron microscopy (TEM), SEM, and EDS using a FEI Tecnai G2 equipped with a 200 kV LaB_6 electron source.

3. Results

3.1. Characterization of the oxide powders

The results of the ICP-AES analyses of U and Mo elemental concentrations in the supernatants collected during the synthesis washing steps and in aliquots from the full dissolution of weighed amounts of the oxide powders are given in Table 1. The yield of precipitation was thus calculated from the concentration of U and Mo in solution and was found to be higher than 98 % for both elements. This shows the efficient and quantitative precipitation of U and Mo via the hydroxide wet-chemistry protocol. Indeed, the molar fraction of the Mo element in the oxide powders was not significantly different from what was expected, and they were both in agreement for all Mo contents (Table 1). After verifying the compositions, the oxide powders containing 0, 0.6, 2, 4, 6, 9, and 15 mol% Mo were used thereafter to prepare sample pellets.

SEM observation of the converted uranium oxide powders containing 0, 2, 4, and 9 mol% Mo is represented in Fig. 1. It showed that the oxide powders obtained after the hydroxide conversion at 1073 K for 4 h under a reducing atmosphere of Ar + 4 % H_2 did not exhibit a well-defined morphology. To add, the oxide powders revealed a similar aspect and appeared to be isomorphic, whatever the considered Mo content. These prepared oxide powders were composed of nanometric particles, as already observed by J. Martinez et al. [20], who studied uranium-cerium oxide solid solutions, where the reported heating treatment at 1073 K for 4 h was sufficient to fully convert the hydroxide precursors into oxides. Accordingly, the hydroxide precipitation of U and Mo followed by calcination led to the formation of nanosized oxide precursors with a strong homogeneity of the initial mixture of elements (Fig. S1).

Table 1
Expected and measured molar fractions of Mo and U by ICP-OES in the samples prepared by hydroxide coprecipitation. The recovery yields of U and Mo were determined by analyzing the supernatants collected during the synthesis washing steps.

$Mo/(Mo+U)_{expected}$ (mol%)	$Mo/(Mo+U)_{ICP-OES}$ (mol%)	Mo Recovery yield (%)	U Recovery yield (%)
0	–	–	99 ± 1
0.6	0.62 ± 0.06	99 ± 1	99 ± 1
2	2.15 ± 0.06	98 ± 1	99 ± 1
4	4.02 ± 0.13	98 ± 1	99 ± 1
6	6.06 ± 0.05	98 ± 1	99 ± 1
9	8.75 ± 0.08	98 ± 2	99 ± 1
15	15.15 ± 0.10	98 ± 2	99 ± 1

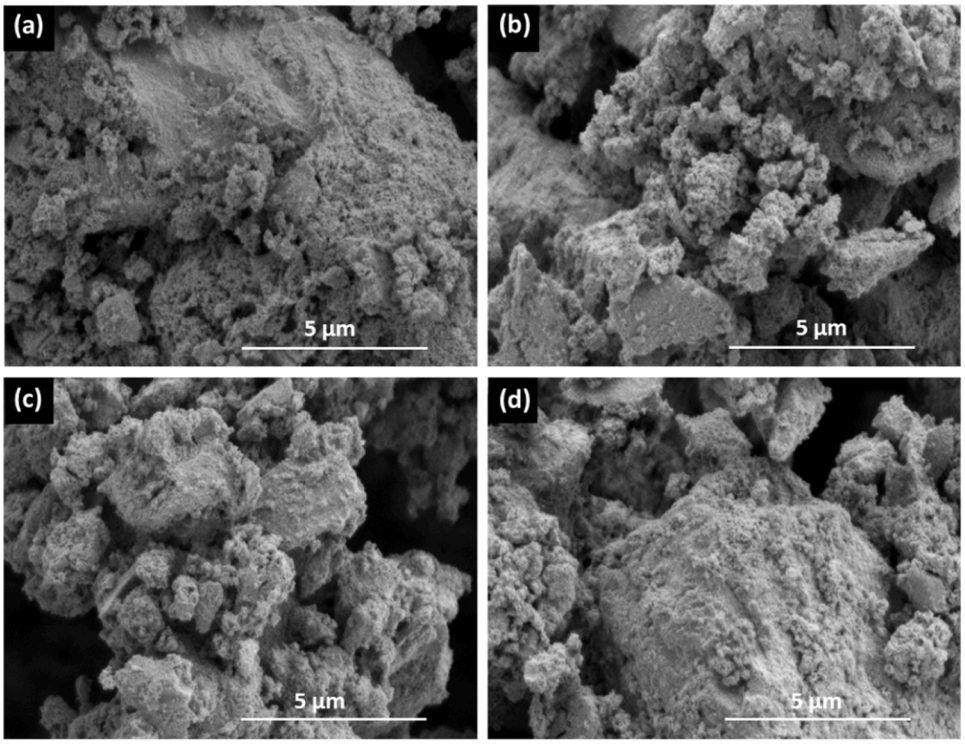

Fig. 1. SEM micrographs of the converted uranium oxide powders containing 0 mol% Mo (a), 2 mol% Mo (b), 4 mol% Mo (c), and 9 mol% Mo (d).

3.2. PXRD analysis of the oxide samples before and after sintering

According to literature, the solubility of Mo in UO_2 varies between 0.006 and 4 mol%. Consequently, after the hydroxide conversion step, one could anticipate the formation of a mixed $(U_{1-y}Mo_y)O_{2\pm x}$ phase ($0.00006 \leq y \leq 0.04$) as well as possible Mo precipitates separated from the $UO_{2\pm x}$ matrix. In order to confirm the obtaining of uranium dioxide and/or to note the appearance of possible Mo secondary phases linked to the addition of Mo and the potential structural changes versus Mo content, the recorded PXRD patterns were indexed during Rietveld refinement considering the UO_2 fluorite-type structure ($Fm\bar{3}m$ space group) and the Mo body-centered cubic structure ($Im\bar{3}m$ space group) in CIF files imported from the Am. Mineralog. Crystal Structure Database (AMCSD) [25]. The latter phase of Mo was chosen based on the fact that under the highly reducing atmosphere of the carried heating treatments, the Mo secondary precipitates (if present) are thermodynamically expected to be stable as a metallic phase with a *bcc*-type structure [26]. In the irradiated spent nuclear fuel, the Mo metallic phase (*bcc*) together with the other metals Ru, Rh, Pd, and Tc form the ε-phase alloy, which mostly exhibits a hexagonal close packed structure (*hcp*) [1,5,10–12].

PXRD analysis of both the oxide powders obtained after calcination at 1073 K for 4 h and from crushed parts of the sintered pellets at 1873 K for 6 h under reducing atmosphere (Ar + 4 % H_2) revealed similar patterns given in Figs. S2 and 2. To elaborate, in the absence of Mo, the PXRD pattern (at the bottom of Fig. 2) shows peaks characteristic of the UO_2 fluorite structure only, where U^{4+} ions occupy the octahedral sites and O^{2-} ions occupy the tetrahedral sites [27]. This pattern was also observed for all the other samples containing different contents of Mo, indicating that they all have the fluorite structure of UO_2. However, only one peak matching the Mo phase was observed around 40.6° (2θ) and became more defined at high Mo contents. This trend was similar to that obtained by Y.K. Ha et al. [15], who presumed the formation of $(U_{1-x}Mo_x)O_2$ solid solution for Mo contents lower than 4 mol% in the absence of observing any other phase. Another plausible explanation could be attributed to the molar fraction of Mo in the powders that was too low to detect any additional phase in UO_2 or identify extra Mo

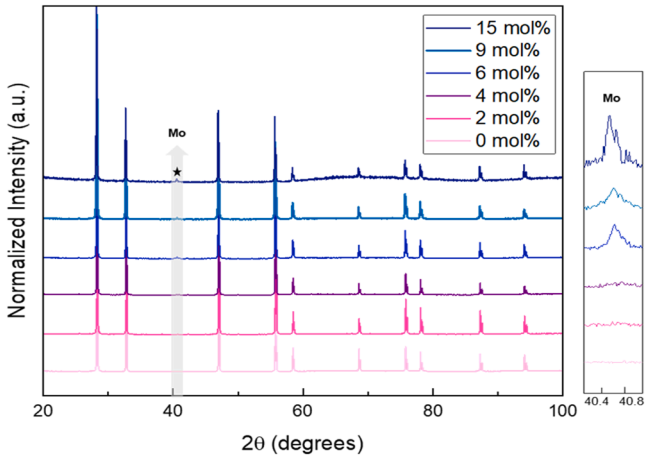

Fig. 2. PXRD patterns obtained after both hydroxide conversion and sintering thermal treatments under reducing atmosphere (Ar + 4 % H_2).

fingerprints at the considered angular range 2θ. To exemplify, recent studies regarding UO_2 containing 3 mol% of platinum-group metals (Ru, Rh, and Pd) did not identify any pattern corresponding to the incorporated platinoid elements at this content by PXRD although they were well-observed as separate metallic segregates at the surface of their sintered UO_2 pellets [28–30].

In addition, the lattice parameter variation of the fluorite structure versus Mo content is illustrated in Fig. 3. The Mo incorporation in UO_2 should have induced a linear variation of the lattice parameter with Mo content following Vegard's law [31]. Such correlation was absent in our case, in which the lattice parameter of the oxide powders obtained after calcination at 1073 K (in black) fluctuated randomly in the studied Mo range between 0 and 15 mol%, while that of the sintered oxide powders at 1873 K (in red) was almost constant or insignificant with Mo content. This indicated that the Mo solubility in the fluorite-type structure is

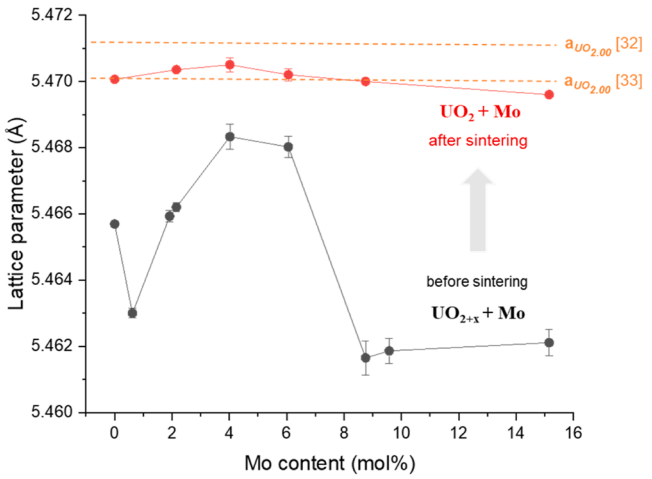

Fig. 3. Calculated lattice parameter values (Å) of the uranium oxide structure obtained after hydroxide conversion (in black) and after sintering (in red) as a function of Mo content (mol%). Examples of lattice parameter measurements of stoichiometric $UO_{2.00}$ are represented in dashed lines: $a = 5.47127 \pm 0.00008$ Å by G. Leinders et al. [32] and $a = 5.4704 \pm 0.0008$ Å by F. Grønvold [33].

almost negligible. Moreover, the lattice parameter value of the calcinated samples is much lower than that reported in the literature for stoichiometric $UO_{2.00}$ [32–36]. This could be explained by the oxygen incorporation in the UO_2 fluorite structure in empty octahedral sites, resulting in hyper-stoichiometric UO_{2+x} phase ($0 < x < 0.25$) of the same crystal structure with slight lattice distortions [27,37], and the random variation observed is dependent on the amount of incorporated oxygen and not on the Mo content. Upon sintering the slightly oxidized samples obtained after calcination at higher temperatures and for a longer duration under reducing atmosphere (Ar + 4 % H_2), the lattice parameter of the fluorite structure becomes close to that estimated for stoichiometric $UO_{2.00}$, such as 5.47127 ± 0.00008 Å by G. Leinders et al. [32] or 5.4704 ± 0.0008 Å by F. Grønvold [33] (Fig. 3). As a result, it can be deduced that Mo has an almost negligible solubility in both stoichiometric and hyper-stoichiometric uranium dioxide matrices and that the sintering step was capable of transforming the hydroxide-converted UO_{2+x} + Mo green pellets into nearly stoichiometric UO_2 + Mo sintered pellets.

3.3. Properties of the sintered UO_2 + Mo pellets

3.3.1. Microstructure of the UO_2 + Mo pellets

In the presence of Mo, the UO_2 microstructure for all the sample compositions obtained following sintering at 1873 K for 6 h under reducing atmosphere revealed the formation of nanosized particles of Mo at the surface of UO_2 grains and within the grain boundaries, as illustrated in Fig. 4. The Mo particles were clearly visible even for contents of 0.6 mol% and 2 mol% Mo in UO_2, as shown in Fig. 4(a) and (b), respectively. This was in agreement with the previous Rietveld refinement results, which indicated that Mo was not incorporated in the UO_2 fluorite structure in the studied range between 0 and 15 mol%. Furthermore, the Mo particles observed were commonly light gray in color but could also be darker (Fig. 4(a)) within the same sample depending on their topographical position at the UO_2 surface and their interaction with the electron beam during data acquisition.

In addition, the microstructure obtained for the prepared pellets was similar to that of the real spent nuclear fuel, with the ε-phase metallic particles of Mo-Ru-Rh-Pd-Tc distributed within the fuel grains and intergranularly with a diameter ranging from a few micrometers to 5–20 nanometers depending on their pellet radial location [1–12]. In this study and upon increasing the Mo content in UO_2, larger Mo particles could be formed at the UO_2 surface as observed in Fig. 4(c)–(e). This could be attributed to the possible coarsening or bonding of smaller nanosized Mo particles driven by diffusion during the sintering step [38,39]. Polishing the sample surfaces to a mirror grade allowed the depiction of an enhanced view of the homogeneous distribution of Mo spherical particles in the UO_2 grains and within the grain boundaries, as

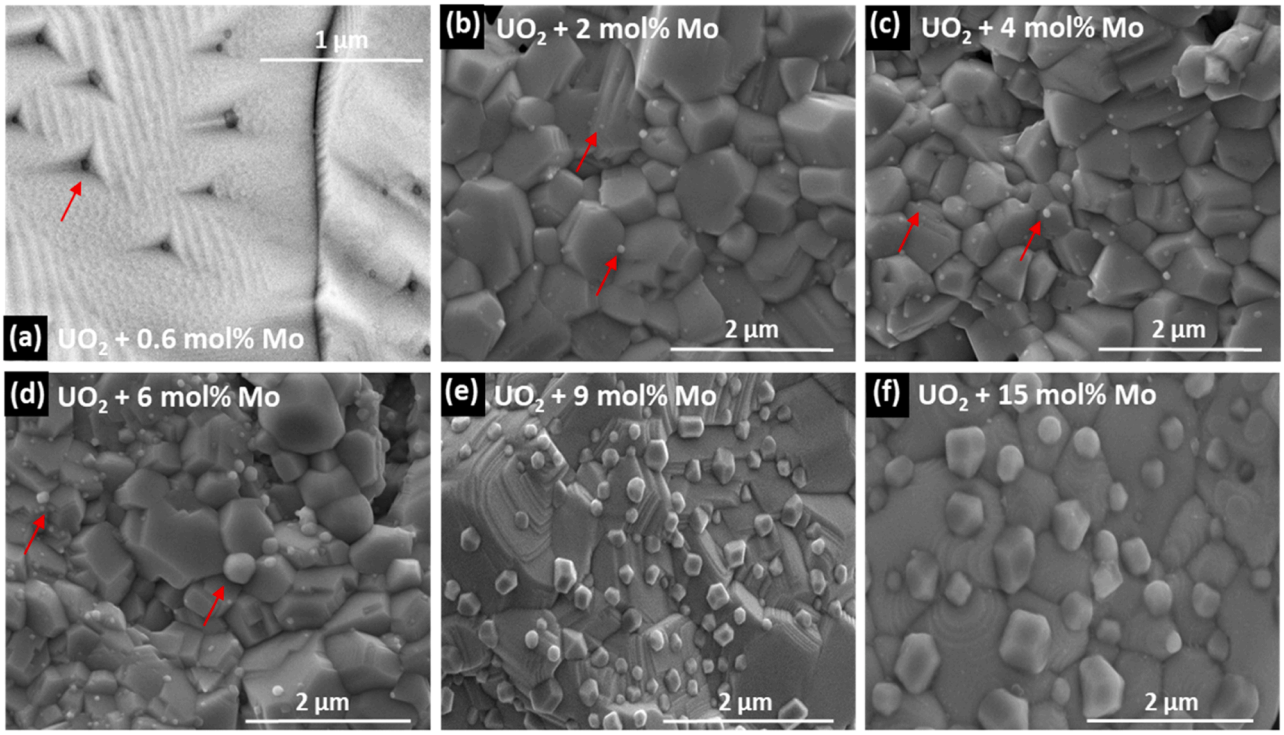

Fig. 4. SEM-SE micrographs showing the presence of Mo particles on the surface of all the sintered UO_2 pellets containing Mo: (a) UO_2+0.6 mol% Mo, (b) UO_2 + 2 mol% Mo, (c) UO_2 + 4 mol% Mo, (d) UO_2 + 6 mol% Mo, (e) UO_2 + 9 mol% Mo, and (f) UO_2 + 15 mol% Mo.

represented in Fig. 5. It is worth noting that the homogeneous dispersion of the Mo particles was not restricted only to the surface of the pellets but was also well-observed in the bulk material too (Fig. S3). Besides, the presence of Mo particles was confirmed by EDS mapping (Fig. 5(a)). However, very small Mo particles (< 10 nm) were hard to detect with the EDS detector although they were visualized during the analyses. The Mo particle size distribution was statistically computed following image processing of various selected zones, as exemplified in Fig. 5, using the Trainable Weka Segmentation plugin in Fiji that allowed the discrete discrimination between UO_2 grains, Mo particles, and pores once the model was optimized. In general, the Mo particle size increased with the Mo content in the UO_2 samples due to the possible coarsening of smaller Mo particles during sintering, as previously mentioned. The bar graphs in Fig. 5 show that the Mo particle size distribution ranges approximately from 5 to 50 nm in UO_2 samples containing 2, 4, and 6 mol% Mo and from 5 to about 100 nm in UO_2 + 9 mol% Mo, hence within the diameter range of the ε-metallic particles in the real spent fuel.

The EDS spectrum in Fig. 6 from one of the Mo particles observed in an ultra-fine cross section from a UO_2 + 2 mol% Mo sintered pellet cut by FIB showed the presence of a high Mo content and a low content of oxygen. Indeed, under the specified reducing conditions during both calcination and sintering heat treatments, Mo was present in the UO_2 samples in the metallic state Mo (0) as expected. Amounts of U and O in the spectrum were detected on account of the surrounding UO_2 grains.

3.3.2. Density and porosity of the UO_2 + Mo pellets

Following the sintering at 1873 K for 6 h under reducing atmosphere (Ar + 4 % H_2), the geometric density of each pellet was measured to determine the densification rate, whereas density measurements by He pycnometry were carried out to evaluate open and closed porosities (Table 2). The geometric densities obtained for the sintered UO_2 pellets containing Mo between 0 and 15 mol% were in the range between 82 and 89 % of the calculated density, with no significant impact of the Mo addition on the density values. The relatively low values of density could be mainly attributed to heating the synthesized hydroxide precursors comprising U and Mo for 4 h under reducing atmosphere at a calcination temperature of 1073 K that lowered powder reactivity. The density could nevertheless be improved by lowering the calcination temperature or increasing the sintering temperature. In addition, the total porosity of the pellets varied approximately between 11 and 18 %, with a major contribution from the open porosity, which was more dominant and higher than the closed porosity in all the sample pellets. A general view of the surface of some sintered pellet samples (before and after polishing) showing open pores is given in Fig. S4.

3.3.3. Impact of Mo addition on UO_2 grain growth

The average grain size of UO_2 shown in Fig. 7 was calculated for the studied UO_2 pellets of different Mo contents between 0 and 15 mol% using the SEraMic method [22] (an example of image processing is given in Fig. S5). It is worth reminding that the studied samples were thermally treated under the same calcination and sintering conditions. In the absence of Mo, the average grain size obtained for pure UO_2 was about 1.8 μm, which was in accordance with that reported by T. Kaczmarek et al. [30] using the hydroxide route and similar thermal treatments for preparing UO_2 (~ 2.5 μm). The average UO_2 grain size was significantly reduced to about 0.45 μm with increasing the Mo content in UO_2 up to 2 mol% and remained relatively constant at this mean value in the UO_2 samples containing higher amounts of Mo up to 15 mol%. This decrease in the UO_2 grain size confirmed that the addition of Mo to UO_2, which manifested in the form of nanosized scattered particles, caused an inhibition of the grain growth in UO_2 during sintering. Consequently, Mo is an antagonist to other doping elements, such as Cr and Mn [40,41], that promote grain growth within UO_2 to obtain enlarged grains in order to slow fission gas release. The microstructure obtained for the UO_2 + Mo pellets was thus similar to that of the real spent nuclear fuel, except that the UO_2 grains were smaller due to Mo addition.

4. Discussion

Contrary to other preparation methods of UO_2 incorporating Mo, such as direct dry mixing of U and Mo precursors or implementation of Mo ions at a certain depth in UO_2, the hydroxide precipitation route starting from U and Mo solutions followed by calcination allowed the formation of mixed U and Mo nanosized precursors with remarkable homogeneity. Thanks to full-dissolution ICP-OES analyses, the chemical composition of the oxide sample powders was verified, and powders of Mo content ranging between 0 and 15 mol% were used to prepare sample pellets. The PXRD patterns in Figs. 2 and S2 showed peaks characteristic of the UO_2 fluorite structure in all the studied samples. However, the weight percentage of Mo in the synthesized samples was quite low (15 mol% is equivalent to about 5 wt% Mo in UO_2) and lied very close to the detection limit of the diffractometer. This is why the diffraction patterns of Mo were of low intensity or absent, even after the sintering step. Nevertheless, the low intensity diffraction peak observed at about 40.6° (2θ) indicated the minor presence of a secondary Mo metallic phase in UO_2. Moreover, the minimum oxygen potential, $\Delta\overline{G}_{O_2} = RT\ln(pO_2)$ required for the formation of stable ternary U-Mo-O oxide phases ($UMoO_6$, U_2MoO_8, $UMoO_5$, UMo_2O_8, UMo_7O_{22}, and $UMo_{11}O_{35}$) according to the study of Chattopadhyay et al. [42] at 1000 K, is about −1425 kJ.mol^{-1} (lowest oxygen potential possible for $UMoO_5$). The oxygen potentials during the calcination heat treatment at 1073 K and the sintering heat treatment at 1873 K under Ar + 4 % H_2 ($pO_2 \approx 10^{-29}$ atm) are of about −596 and −1040 kJ.mol^{-1}, respectively. Consequently, none of the ternary oxides is expected to form in the prepared samples. Furthermore, if Mo were soluble in the fluorite structure, this would have induced a linear variation of the lattice parameter as a function of Mo content. Nevertheless, such correlation was absent in the case of the hyper-stoichiometric UO_{2+x} samples after calcination with a random variation of the lattice parameter between 5.641 and 5.649 Å, depending rather on the amount of oxygen incorporated. It was also absent in the case of the stoichiometric UO_2 samples obtained after sintering with a nearly constant lattice parameter of about 5.47 Å, independent of the Mo content. This implies that Mo has a negligible solubility in the fluorite structures of UO_2 and UO_{2+x} following the applied thermal treatments. The plotted Ellingham diagram in Fig. 8 shows the oxygen potential equilibrium values of $UO_{2\pm x}$ based on thermodynamic data equations derived from T.B. Lindemer and T.M. Besmann [43], along with the oxygen potentials corresponding to the Mo/MoO_2 equilibrium based on the approximations calculated by J. Bygdén et al. [26]. Under the highly reducing conditions, particularly of the sintering step of the pellets prepared from the oxide powders, Mo should be thermodynamically stable as a metallic phase Mo (0), crystallizing in the bcc-type structure. Therefore, the only two existing phases expected in the prepared pellets following the sintering heat treatment are Mo (0) and nearly stoichiometric UO_2.

Although the maximum solubility limit of Mo in UO_2 proposed by Ha et al. [15] is as high as 4 mol% Mo, we were able to detect the appearance of nanosized metallic Mo nanoparticles for all the studied compositions, even for lower contents of 2 and 0.6 mol% Mo. This confirms that the Mo solubility is rather below 0.6 mol% Mo and very likely to be negligible, as predicted by the Rietveld refinement results. The produced UO_2 + Mo pellets were free from cracks and manifested congruence in terms of density and porosity with no significant impact provoked by Mo addition, apart from the decrease in UO_2 grain size due to the Mo inhibition of UO_2 grain growth during the sintering thermal treatment. The mechanism of UO_2 grain growth retardation with increasing Mo content could be explained by the solute drag effect. The existence of Mo particles (solute) at the grain boundaries, even in small amounts due to its negligible solubility, could lead to a decrease in grain boundary mobility. Whereas other dopants like Cr or Mn, which can dissolve significantly in the UO_2 fuel matrix, have a positive impact on UO_2 grain growth [40,41].

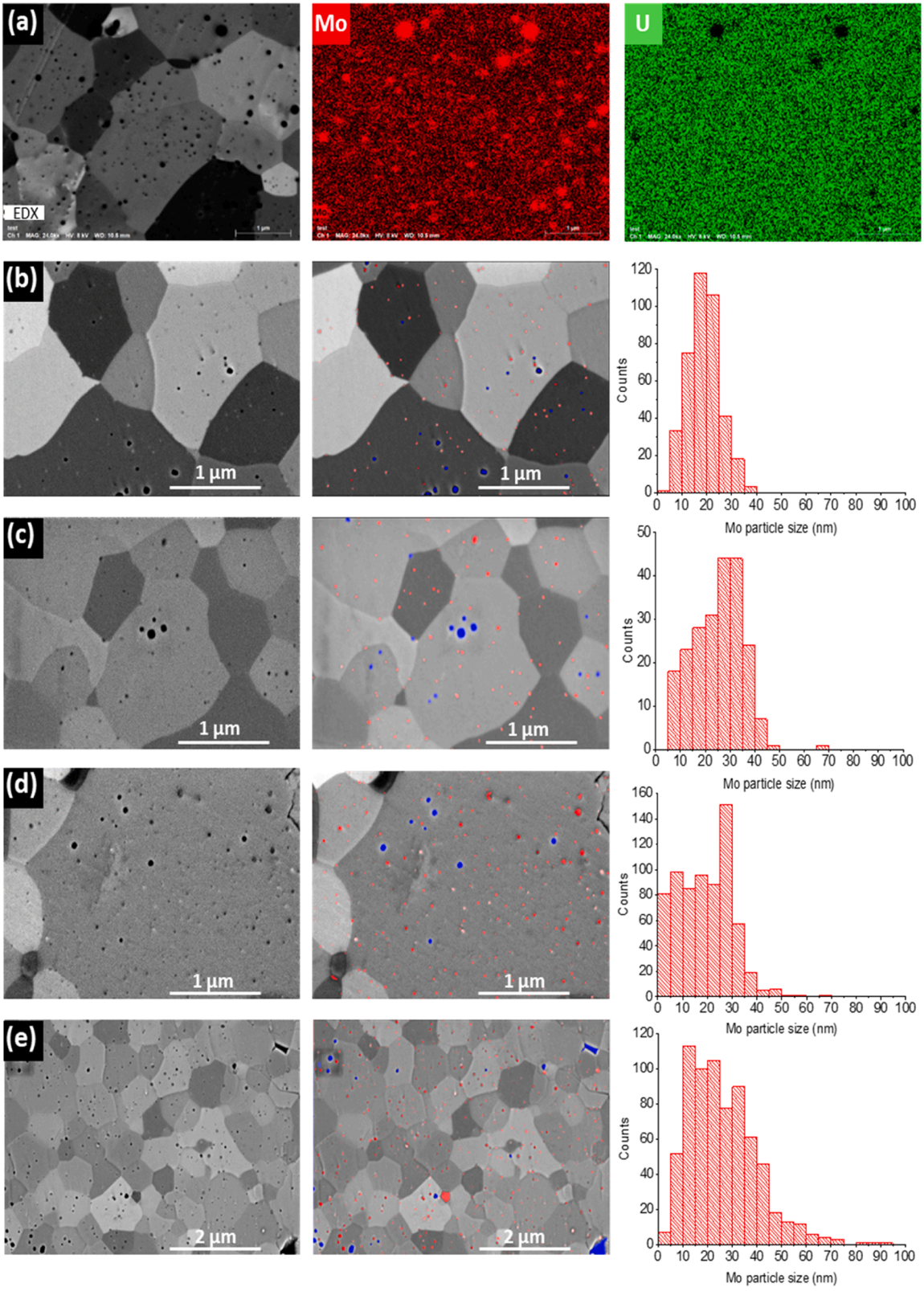

Fig. 5. (a) EDS mapping images of a polished UO_2 + 9 mol% Mo sample pellet; (b), (c), (d), and (e): high magnification SEM-BSE image examples recorded at 3 kV of selected zones in the polished samples for determining Mo particle size distribution by Trainable Weka Segmentation at Mo contents 2, 4, 6, and 9 mol% in UO_2, respectively. The Mo particles are red-colored, and the pores are blue-colored.

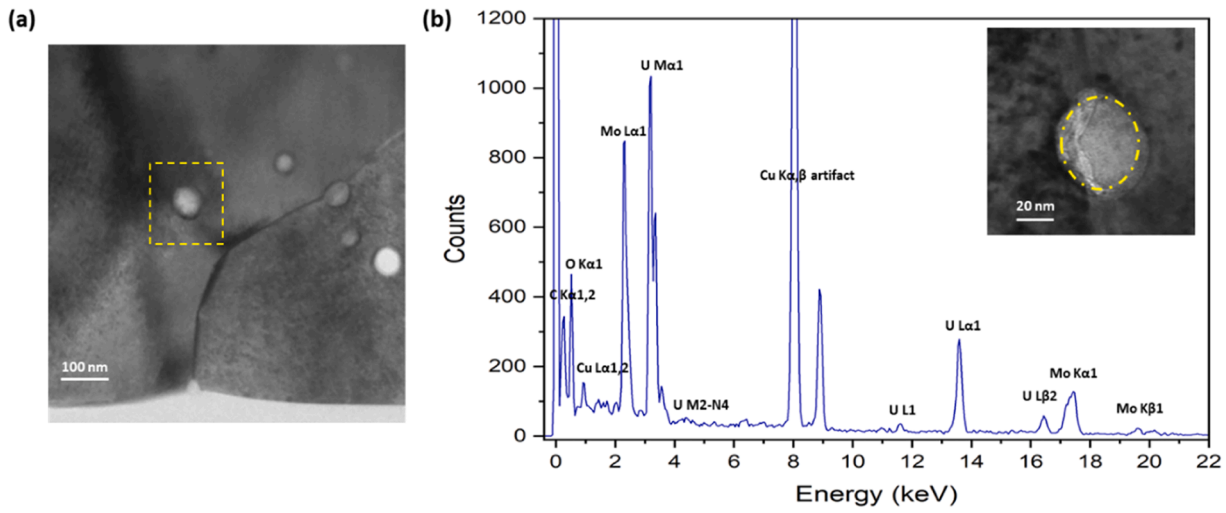

Fig. 6. (a) TEM image showing Mo particles in a FIB lamella cut from UO_2 + 2 mol% Mo sintered pellet on a copper grid coated with lacey carbon; (b) EDS spectrum of the highlighted Mo particle.

Table 2
Density and porosity measurements of the prepared UO_2 pellets containing Mo between 0 and 15 mol% following sintering at 1873 K for 6 h under reducing atmosphere (Ar + 4 % H_2).

Pellet composition	d_{geo}/d_{calc} (%)	d_{pycno}/d_{calc} (%)	P_{closed} (%)	P_{open} (%)
UO_2	83 ± 1	99 ± 1	0 ± 1	17 ± 1
UO_2 + 0.6 mol% Mo	82 ± 2	99 ± 1	1 ± 1	17 ± 1
UO_2 + 2 mol% Mo	87 ± 1	98 ± 2	2 ± 1	11 ± 1
UO_2 + 4 mol% Mo	88 ± 2	99 ± 1	1 ± 1	11 ± 1
UO_2 + 6 mol% Mo	89 ± 1	95 ± 1	5 ± 1	6 ± 1
UO_2 + 9 mol% Mo	84 ± 1	97 ± 2	3 ± 1	10 ± 2
UO_2 + 15 mol% Mo	82 ± 2	99 ± 1	1 ± 1	17 ± 1

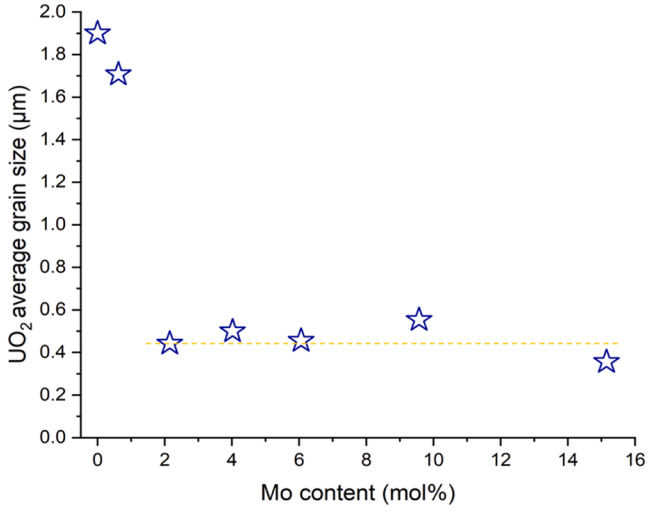

Fig. 7. Variation of the UO_2 average grain size (μm) with Mo addition (mol%).

As a matter of interest, the Mo nanoparticles were homogeneously distributed throughout the entire sample pellets, with a spherical geometry and a diameter in the range of 5–50 nm in the UO_2 samples containing 2, 4, and 6 mol% Mo and 5–100 nm in UO_2 + 9 mol% Mo, where an increase in the Mo particle size with Mo content might be induced by particle coarsening during sintering. All in all, such simplified UO_2-based model compounds incorporating Mo nanoparticles mimic the real spent nuclear fuel with the ε-phase metallic nanoparticles with regards to the microstructure, except that the UO_2 grains are smaller. Later, these simplified model compounds can be utilized in order to study the specific impact of the metallic Mo phase, representing the major component of the ε-phase, on the long-term behavior of the irradiated fuel in geological repositories or on the kinetics of dissolution of the spent fuel during reprocessing.

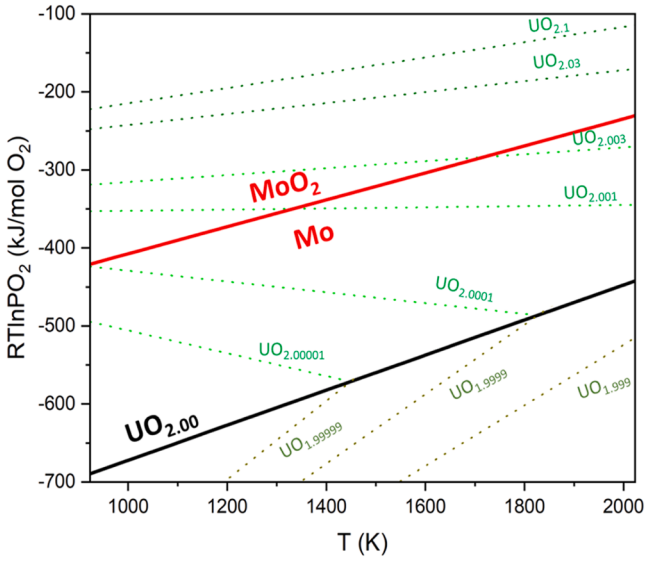

Fig. 8. Ellingham diagram showing the Mo/MoO_2 (data from [26]) equilibrium oxygen potentials with several $UO_{2\pm x}$ examples (data from [43]), including exact $UO_{2.00}$.

5. Conclusion

In this study, we used a wet chemistry route to prepare UO_2-based model compounds with various Mo contents between 0 and 15 mol% by hydroxide precipitation in order to investigate the behavior of Mo in $UO_{2\pm x}$. Although the previous studies suggested a Mo solubility range between 0.006 and 4 mol% in UO_2, PXRD analyses and Rietveld refinement calculations performed in this work indicate that Mo has a negligible solubility in the fluorite structure of both UO_2 and UO_{2+x}. Analyses of the produced UO_2 + Mo sintered pellets by SEM, TEM, and EDS showed the presence of nanosized Mo particles of metallic nature homogeneously distributed at the UO_2 surface and within the grain

boundaries, even for a relatively low content of 0.6 mol% in UO_2. Thus, the solubility threshold of Mo in UO_2 is undoubtedly way lower than that suggested by Ha et al. [15] of 4 mol% Mo. Furthermore, the Mo addition to UO_2 induced an inhibition of the UO_2 grain growth during sintering, and the obtained UO_2 + Mo pellets had thus smaller UO_2 grains compared to those in pure UO_2 pellets or pellets incorporating Mo at contents below 2 mol%. In addition, the produced UO_2 pellets doped with Mo metallic nanoparticles exhibit a microstructure similar to that of the real spent nuclear fuel with ε-phase metallic nanoparticles. The Mo metallic nanoparticles in these simplified UO_2-based model compounds of controlled microstructure could be harnessed as surrogates of the Mo-rich ε-phase metallic nanoparticles in the real spent nuclear fuel for other studies in the future regarding the specific impact of the Mo on waste management.

CRediT authorship contribution statement

Mohammad Husainy: Writing – original draft, Investigation, Data curation. **Stéphanie Szenknect:** Writing – original draft, Writing – review & editing, Investigation, Supervision, Validation. **Renaud Podor:** Writing – original draft, Investigation. **Xavier Le Goff:** Writing – original draft, Software, Investigation. **Thibault Kaczmarek:** Investigation, Data curation. **Philippe Moisy:** Writing – original draft, Validation, Supervision, Funding acquisition. **Nicolas Dacheux:** Supervision, Funding acquisition, Validation, Writing – original draft, Writing – review & editing.

Declaration of competing interest

The authors declare that they have no known competing financial interests or personal relationships that could have appeared to influence the work reported in this paper.

Data availability

Data will be made available on request.

Acknowledgements

This work is part of the PhD thesis of M. Husainy and received funding from the CEA. The authors would like to thank Joseph Lautru (ICSM Marcoule) for his support during SEM measurements. The authors would also like to acknowledge Martiane Cabié (CP2M Aix-Marseille University) for her support in FIB lamellae preparation and investigation.

Supplementary materials

Supplementary material associated with this article can be found, in the online version, at doi:10.1016/j.jnucmat.2024.155075.

References

[1] H. Kleykamp, The chemical state of the fission products in oxide fuels, J. Nucl. Mater. 131 (1985) 221–246, https://doi.org/10.1016/0022-3115(85)90460-X.
[2] B. Lewis, W.T. Thompson, F.C. Iglesias, Fission product chemistry in oxide fuels, Compreh. Nucl. Mater. 2 (2012) 515–546, https://doi.org/10.1016/B978-0-08-056033-5.00042-2.
[3] P.C. Burns, R.C. Ewing, A. Navrotsky, Nuclear fuel in a reactor accident, Science 335 (2012) 1184–1188, https://doi.org/10.1126/science.1211285.
[4] FranceJ.-F. Parisot (Ed.), Nuclear Fuels, Éditions le Moniteur: CEA, Paris, 2009.
[5] H. Kleykamp, J.O. Paschoal, R. Pejsa, F. Thümmler, Composition and structure of fission product precipitates in irradiated oxide fuels: correlation with phase studies in the Mo-Ru-Rh-Pd and BaO-UO2-ZrO2-MoO2 Systems, J. Nucl. Mater. 130 (1985) 426–433, https://doi.org/10.1016/0022-3115(85)90329-0.
[6] Ch. Poinssot, P. Toulhoat, J.P. Grouiller, J. Pavageau, J.P. Piron, M. Pelletier, Ph. Dehaudt, Ch. Cappelaere, R. Limon, L. Desgranges, Ch. Jegou, C. Corbel, S. Maillard, M.H. Faure, J.C. Cicariello, M. Masson, Synthesis on the Long Term Behavior of Spent Nuclear Fuel, 1, 2001. CEA-R-5958(E).
[7] S. Nicoll, H. Matzke, R.W. Grimes, C.R.A. Catlow, The behaviour of single atoms of molybdenum in urania, J. Nucl. Mater. 240 (1997) 185–195, https://doi.org/10.1016/S0022-3115(96)00716-7.
[8] P. Martin, M. Ripert, G. Carlot, P. Parent, C. Laffon, A study of molybdenum behaviour in UO2 by X-ray absorption spectroscopy, J. Nucl. Mater. 326 (2004) 132–143, https://doi.org/10.1016/j.jnucmat.2004.01.006.
[9] E. Buck, B. Hanson, B. Mcnamara, The geochemical behaviour of Tc, Np and Pu in spent nuclear fuel in an oxidizing environment, in: Energy, Waste, and the Environment: A Geochemical Perspective: The Geological Society, 236, Special Publications, London, 2004, pp. 65–68, https://doi.org/10.1144/GSL.SP.2004.236.01.05.
[10] R.A. Clark, M.A. Conroy, T.G. Lach, E.C. Buck, K.L. Pellegrini, B.K. McNamara, J. M. Schwantes, Distribution of metallic fission-product particles in the cladding liner of spent nuclear fuel, Npj Mater. Degrad. 4 (2020) 1–9, https://doi.org/10.1038/s41529-019-0107-0.
[11] E.C. Buck, E.J. Mausolf, B.K. McNamara, C.Z. Soderquist, J.M. Schwantes, Nanostructure of metallic particles in light water reactor used nuclear fuel, J. Nucl. Mater. 461 (2015) 236–243, https://doi.org/10.1016/j.jnucmat.2015.03.001.
[12] D. Cui, V.V. Rondinella, J.A. Fortner, A.J. Kropf, L. Eriksson, D.J. Wronkiewicz, K. Spahiu, Characterization of alloy particles extracted from spent nuclear fuel, J. Nucl. Mater. 420 (2012) 328–333, https://doi.org/10.1016/j.jnucmat.2011.10.015.
[13] H. Kleykamp, The solubility of selected fission products in UO2 and (U, Pu)O2, J. Nucl. Mater. 206 (1993) 82–86, https://doi.org/10.1016/0022-3115(93)90236-R.
[14] G. Giacchetti, C. Sari, Behavior of molybdenum in mixed-oxide fuel, Nucl. Technol. 31 (1976) 62–69, https://doi.org/10.13182/NT76-A31699.
[15] Y.K. Ha, J.G. Kim, Y.S. Park, S.D. Park, K.S. Song, Behaviors of molybdenum in UO2 fuel matrix, Nucl. Eng. Technol. 43 (2011) 309–316.
[16] L. Sarrasin, Mécanismes D'incorporation Et De Migration Du Molybdène Dans Le Dioxyde D'uranium Stoechiométrique Et Sur-Stoechiométrique, Université de Lyon, 2017 phdthesis, https://theses.hal.science/tel-01743739.
[17] L. Sarrasin, C. Gaillard, C. Panetier, Y. Pipon, N. Moncoffre, D. Mangin, R. Ducher, R. Dubourg, Effect of the Oxygen Potential on the Mo Migration and Speciation in UO2 and UO2+x, Inorg. Chem. 58 (2019) 4761–4773, https://doi.org/10.1021/acs.inorgchem.8b03076.
[18] E.C. Corcoran, J.-L. Flèche, N. Dupin, B. Sundman, C. Guéneau, Thermodynamic investigations of the uranium-molybdenum-oxygen system by a coupling of density functional theory and CALPHAD methodologies, Calphad 63 (2018) 196–211, https://doi.org/10.1016/j.calphad.2018.10.002.
[19] M. Khair, Oxydo-réduction et spéciation des produits de fission corrosifs dans les combustibles oxydes. Évaluation des bénéfices d'un combustible tamponné en pO2, 2019.
[20] J. Martinez, N. Clavier, A. Mesbah, F. Audubert, X.F. Le Goff, N. Vigier, N. Dacheux, An original precipitation route toward the preparation and the sintering of highly reactive uranium cerium dioxide powders, J. Nucl. Mater. 462 (2015) 173–181, https://doi.org/10.1016/j.jnucmat.2015.03.053.
[21] B.H. Toby, R.B. Von Dreele, *GSAS-II* : the genesis of a modern open-source all purpose crystallography software package, J. Appl. Crystallogr. 46 (2013) 544–549, https://doi.org/10.1107/S0021889813003531.
[22] R. Podor, X.Le Goff, J. Lautru, H.P. Brau, M. Massonnet, N. Clavier, SEraMic: a semi-automatic method for the segmentation of grain boundaries, J. Eur. Ceram. Soc. 41 (2021) 5349–5358, https://doi.org/10.1016/j.jeurceramsoc.2021.03.062.
[23] J. Schindelin, I. Arganda-Carreras, E. Frise, V. Kaynig, M. Longair, T. Pietzsch, S. Preibisch, C. Rueden, S. Saalfeld, B. Schmid, J.-Y. Tinevez, D.J. White, V. Hartenstein, K. Eliceiri, P. Tomancak, A. Cardona, Fiji: an open-source platform for biological-image analysis, Nat. Method. 9 (2012) 676–682, https://doi.org/10.1038/nmeth.2019.
[24] I. Arganda-Carreras, V. Kaynig, C. Rueden, K.W. Eliceiri, J. Schindelin, A. Cardona, H.S. Seung, Trainable Weka Segmentation: a machine learning tool for microscopy pixel classification, Bioinformatics 33 (2017) 2424–2426, https://doi.org/10.1093/bioinformatics/btx180.
[25] R.T. Downs, M. Hall-Wallace, The Am. Mineralog. crystal structure database, Am. Mineralog. 88 (2003) 247–250.
[26] J. Bygdén, D. Sichen, S. Seetharaman, A thermodynamic study of the molybdenum-oxygen system, Metall. Mater. Trans. B. 25 (1994) 885–891, https://doi.org/10.1007/BF02662770.
[27] B.T.M. Willis, Structures of UO2, UO2+x andU4O9 by neutron diffraction, J. Phys. France 25 (1964) 431–439, https://doi.org/10.1051/jphys:01964002505043100.
[28] T. Cordara, Effet de la présence de produits de fission sur les mécanismes de dissolution de composés modèles à base de dioxyde d'uranium, These de doctorat, Université de Montpellier, 2017. https://www.theses.fr/2017MONTT176.
[29] T. Cordara, S. Szenknect, R. Podor, V. Trillaud, L. Claparede, X.Le Goff, A. Mesbah, C. Lavalette, N. Dacheux, Microstructural evolution of UO2 pellets containing metallic particles of Ru, Rh and Pd during dissolution in nitric acid solution: 3D-ESEM monitoring, Hydrometallurgy 188 (2019) 182–193, https://doi.org/10.1016/j.hydromet.2019.07.001.
[30] T. Kaczmarek, Impact Des éléments platinoïdes Et Du Molybdène Dans Les Mécanismes De Dissolution Du Dioxyde D'uranium, Université de Montpellier, 2022 phdthesis, https://theses.hal.science/tel-03773114.
[31] L. Vegard, Die Konstitution der Mischkristalle und die Raumfüllung der Atome, Zeitschrift Fur Physik 5 (1921) 17–26, https://doi.org/10.1007/BF01349680.

[32] G. Leinders, T. Cardinaels, K. Binnemans, M. Verwerft, Accurate lattice parameter measurements of stoichiometric uranium dioxide, J. Nucl. Mater. 459 (2015) 135–142, https://doi.org/10.1016/j.jnucmat.2015.01.029.
[33] F. Grønvold, High-temperature X-ray study of uranium oxides in the UO2U3O8 region, J. Inorgan. Nucl. Chem. 1 (1955) 357–370, https://doi.org/10.1016/0022-1902(55)80046-2.
[34] T. Cardinaels, J. Hertog, B. Vos, L. de Tollenaere, C. Delafoy, M. Verwerft, Dopant solubility and lattice contraction in gadolinia and gadolinia–chromia doped UO2 fuels, J. Nucl. Mater. 424 (2012) 289–300, https://doi.org/10.1016/j.jnucmat.2012.02.014.
[35] L. Lynds, W.A. Young, J.S. Mohl, G.G. Libowitz, X-ray and density study of nonstoichiometry in uranium oxides. Nonstoichiometric Compounds, American Chemical Society, 1963, pp. 58–65, https://doi.org/10.1021/ba-1964-0039.ch005.
[36] V.A. Alekseyev, L.A. Anan'yeva, R.P. Rafal'skiy, Effects of Composition on Lattice Parameter of uo2+x, Int. Geol. Rev. 23 (1981) 1229–1236, https://doi.org/10.1080/00206818109451000.
[37] J.M. Elorrieta, L.J. Bonales, N. Rodríguez-Villagra, V.G. Baonza, J. Cobos, A detailed Raman and X-ray study of UO2+x oxides and related structure transitions, Phys. Chem. Chem. Phys. 18 (2016) 28209–28216, https://doi.org/10.1039/C6CP03800J.
[38] R.M. German, Thermodynamics of sintering. Sintering of Advanced Materials, Elsevier, 2010, pp. 3–32, https://doi.org/10.1533/9781845699949.1.3.
[39] Z.Z. Fang, H. Wang, V. Kumar, Coarsening, densification, and grain growth during sintering of nano-sized powders—a perspective, Int. J. Refract. Metal. Hard Mater. 62 (2017) 110–117, https://doi.org/10.1016/j.ijrmhm.2016.09.004.
[40] S. Finkeldei, R.D. Hunt, J.O. Kiggans Jr, C.A. Hobbs, B.D. Eckhart, J.W. Mcmurray, D. Brown, G.W. Helmreich, K.A. Terrani, A. Nelson, Synthesis and Characterization of UO2 Feedstocks containing Controlled Dopants, 2019, https://doi.org/10.2172/1495946.
[41] T. Cardinaels, K. Govers, B. Vos, S. Van den Berghe, M. Verwerft, L. de Tollenaere, G. Maier, C. Delafoy, Chromia doped UO2 fuel: investigation of the lattice parameter, J. Nucl. Mater. 424 (2012) 252–260, https://doi.org/10.1016/j.jnucmat.2012.02.025.
[42] G. Chattopadhyay, S.n. Tripathi, A.s. Kerkar, Thermodynamic investigations in the system U-Mo-O, J. Am. Ceram. Soc. 67 (1984) 610–614, https://doi.org/10.1111/j.1151-2916.1984.tb19604.x.
[43] T.B. Lindemer, T.M. Besmann, Chemical thermodynamic representation of UO2 ± x, J. Nucl. Mater. 130 (1985) 473–488, https://doi.org/10.1016/0022-3115(85)90334-4.